VOLUME 140   JANUARY 2014   ISSN 0034-4257

ELSEVIER

Remote Sensing of Environment

http://www.elsevier.com/locate/rse

Generation of a time-consistent land surface temperature product from MODIS data

Si-Bo Duan [a,b,c], Zhao-Liang Li [d,c,*], Bo-Hui Tang [a], Hua Wu [a], Ronglin Tang [a]

[a] State Key Laboratory of Resources and Environment Information System, Institute of Geographic Sciences and Natural Resources Research, Chinese Academy of Sciences, Beijing 100101, China
[b] University of Chinese Academy of Sciences, Beijing 100049, China
[c] ICube, UdS, CNRS, 300 Bld Sebastien Brant, BP10413, 67412 Illkirch, France
[d] Key Laboratory of Agri-informatics, Ministry of Agriculture/Institute of Agricultural Resources and Regional Planning, Chinese Academy of Agricultural Sciences, Beijing 100081, China

ABSTRACT

Land surface temperature (LST) is crucial for a wide variety of land–atmosphere studies. A long-term and time-consistent LST product is highly desirable for use in global climate studies. In this study, we developed a method to normalize the Terra-MODIS LST during daytime to a consistent local solar time to generate a time-consistent LST product. A multiple linear regression model for the slope of LST versus the local solar time during the period 10:00–12:00 as a function of the normalized-difference vegetation index, solar zenith angle, and digital elevation model was established using MSG-SEVIRI data. The regression equation was then applied to normalize the Terra-MODIS LST during daytime to a consistent local solar time (i.e., 11:00 local solar time). The accuracy of the proposed method was evaluated using MSG-SEVIRI-derived LST data. The results indicate that the root mean square error of the differences between the LST before temporal normalization and the actual LST (derived from MSG-SEVIRI data) is approximately 1.5 K, whereas those between the LST after temporal normalization and the actual LST is approximately 0.5 K.

1. Introduction

Land surface temperature (LST), which is a key variable in the physical processes of land surface energy and water balance on regional and global scales, is widely used in a range of hydrological, meteorological, and climatological applications (Anderson et al., 2008; Karnieli et al., 2010; Li et al., 2009). Satellite remote sensing offers the only possibility to measure LST over extended regions with high temporal and spatial resolution (Li & Becker, 1993; Li, Tang, et al., 2013a). To date, one of the highest-quality LST products has been generated from the Moderate-Resolution Imaging Spectroradiometer (MODIS) onboard the Terra and Aqua platforms (Wan, 2008; Wan, Zhang, Zhang, & Li, 2002, 2004).

Two MODIS LST algorithms were developed to generate the MODIS LST products. One algorithm is the generalized split-window algorithm (Becker & Li, 1990; Wan & Dozier, 1996), which generates LST data at 1 km resolution. The other algorithm is the physics-based day/night algorithm (Wan & Li, 1997), which generates LST data at approximately 5 km (Collection 4) and 6 km (Collection 5) resolution. Two different methods were used to validate the MODIS LST products: a temperature-based method (Wan, 2008; Wan et al., 2002, 2004; Wang, Liang, & Meyers, 2008) and a radiance-based method (Coll, Wan, & Galve, 2009;

Wan & Li, 2008). Comparisons between the MODIS LST products and in situ measurements indicate that the accuracy of the MODIS LST products is better than 1 K for a given observation time and angle. Therefore, the MODIS LST products have been widely used in various studies (Friedl et al., 2010; Tang & Li, 2008; Tang, Li, & Tang, 2010; Wang et al., 2005).

Due to the intrinsic scanning characteristics of the MODIS instrument onboard the polar-orbiting satellites, the differences in local solar time for pixels along a given scan line on the same day (see Fig. 1a) or for the same pixel on different days in one revisit period (see Fig. 1b) may reach up to 2 h. As LST changes with local solar time, it is therefore not possible to directly compare the LST of different pixels on the same day or of the same pixel on different days. Fig. 2 displays LST versus local solar time during the period 10:00–12:00 for in situ data and data from the Meteosat Second-Generation Spinning-Enhanced Visible and Infrared Imager (MSG-SEVIRI) for various land cover types. One hour of differences in local solar time during the period 10:00–12:00 corresponds to LST differences of approximately 3–5 K. Table 1 shows the detailed information and statistics for the data displayed in Fig. 2. To make the LST of different pixels on the same day or of the same pixel on different days comparable, it is therefore necessary to normalize LST to a consistent local solar time to generate a time-consistent LST product. A long-term and time-consistent LST dataset is highly desirable for use in global climate studies (Jin & Dickinson, 2002).

Various methods related to the temporal normalization of LST have been developed using the diurnal cycle of LST. If the diurnal cycle of LST is available, LST at any time can be derived in terms of a diurnal

* Corresponding author at: Key Laboratory of Agri-informatics, Ministry of Agriculture/Institute of Agricultural Resources and Regional Planning, Chinese Academy of Agricultural Sciences, Beijing 100081, China. Tel.: +86 1082105077.
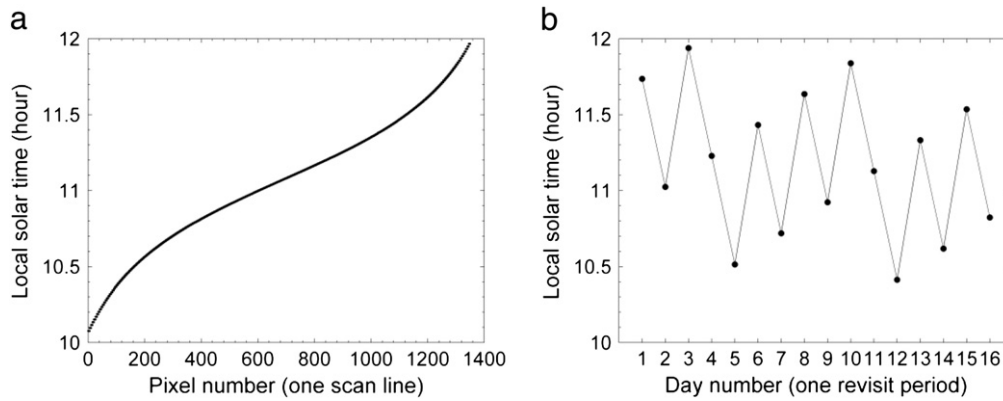E-mail address: lizhaoliang@caas.cn (Z.-L. Li).

Fig. 1. Local solar time (a) for pixels in one MODIS scan line (1354 pixels) and (b) for the same pixel in one MODIS revisit period.

temperature cycle (DTC) model (Duan, Li, Wang, Wu, & Tang, 2012; Göttsche & Olesen, 2001, 2009; Schädlich, Göttsche, & Olesen, 2001). Jin and Dickinson (1999) developed an algorithm to estimate the diurnal cycle of LST by interpolating twice-per-day measurements taken by the National Oceanic and Atmospheric Administration (NOAA) Advanced Very-High-Resolution Radiometer (AVHRR) into the typical patterns of the diurnal LST cycle under cloud-free conditions. These typical patterns are derived from climatology modeled as a function of vegetation types, soil moisture, seasons, and altitude. Therefore, information about vegetation types, soil moisture, and cloud conditions is required to determine the typical pattern of each pixel. This method has also been applied to normalize the NOAA-AVHRR LST with orbit drift effect to a consistent local solar time (Jin & Treadon, 2003). Sun and Pinker (2005) performed work similar to that of Jin and Dickinson (1999), but the typical patterns of the diurnal LST cycle were derived from Geostationary Operational Environmental Satellite (GOES) measurements, rather than those from modeled climatology. Nevertheless, accurate LST retrievals from GOES data for the purpose of obtaining the typical patterns of the diurnal LST cycle remain difficult because of atmospheric effects and the spectral variation of surface emissivity (Li, Wu, et al., 2013b). A similar method has been developed by Mialon, Royer, Fily, and Picard (2007) to interpolate satellite-derived LST from the diurnal cycle of 40-yr European Centre for Medium-Range Weather Forecasts (ECMWF) reanalysis (ERA-40) temperatures. Aires, Prigent, and Rossow (2004) proposed a temporal interpolation algorithm to estimate the diurnal cycle of LST using a principal component analysis decomposition and an iterative optimization algorithm. However, this algorithm is based on 3-hour LST estimates by the International Satellite Cloud Climatology Project (ISCCP), from infrared measurements collected by polar-orbiting and geostationary satellites. Inamdar, French,

Hook, Vaughan, and Luckett (2008) developed an algorithm combining GOES and MODIS data to estimate the diurnal cycle of LST on a 1-km spatial scale. However, the diurnal cycle of LST at a 1-km resolution is disaggregated from that at a 5-km resolution, using the relationship between LST and the normalized-difference vegetation index (NDVI). The disaggregation method has been further improved using surface emissivity data (Inamdar & French, 2009).

The methods described above can be applied to the normalization of LST to a consistent local solar time. However, these methods require the typical patterns of the diurnal LST cycle, which are derived from climate models or satellite measurements. Therefore, a simple and straightforward method for the temporal normalization of LST is needed. The objective of this study is to develop a method to normalize the Terra-MODIS LST during daytime to a consistent local solar time to generate a time-consistent LST product. This method only requires that there be no cloud contamination during the period 10:00–12:00 local solar time, rather than nearly clear-sky conditions throughout the day. This paper is organized as follows: Section 2 describes the study area and the data used in this study. Section 3 describes the method for the temporal normalization of LST. The results and discussion are presented in Section 4. Conclusions are presented in the last section.

2. Study area and data

2.1. Study area

The study area extends from 15° W to 15° E longitude and 30° N to 48° N latitude. This area is in the Mediterranean region and has a Mediterranean climate, with mild, rainy winters and hot, dry summers. The land cover types of the study area are shown in Fig. 3. This area is characterized by barren or sparsely vegetated lands, croplands, and
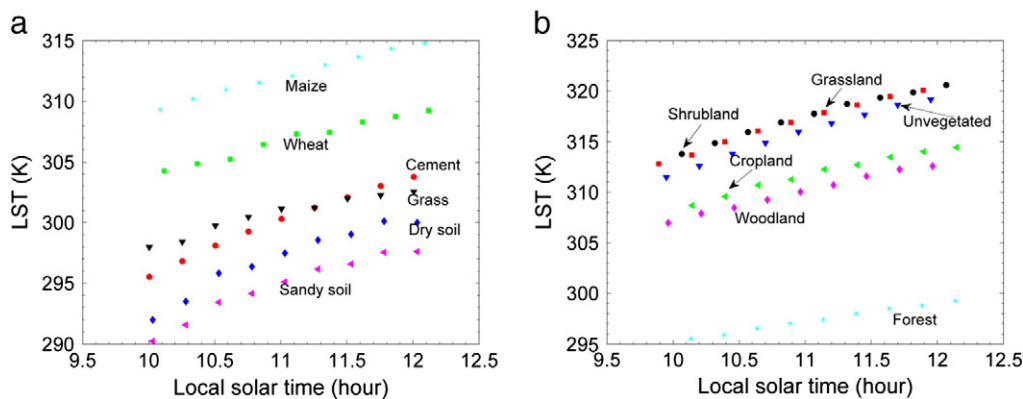

Fig. 2. Land surface temperature versus local solar time during the period 10:00–12:00 for (a) in situ and (b) MSG-SEVIRI-derived LST for different land cover types.

Table 1
Detailed information and statistics for the data displayed in Fig. 2.

Land cover type	Longitude	Latitude	Date	SLP^a	R^{2b}	STD (K)[c]
Cement	119.832 W	34.452 N	22 Feb 2003	4.10	0.99	0.24
Grass	119.833 W	34.452 N	22 Feb 2003	2.33	0.95	0.34
Dry soil	116.611 E	39.603 N	27 Oct 2008	4.04	0.94	0.63
Sandy soil	116.611 E	39.603 N	27 Oct 2008	3.71	0.96	0.50
Maize	0.125 E	44.323 N	16 Jun 1996	2.74	1.00	0.11
Wheat	0.268 E	43.825 N	16 Jun 1996	2.59	0.98	0.22
Forest	0.954 W	42.454 N	31 Jul 2010	1.90	1.00	0.09
Shrubland	2.005 W	33.872 N	31 Jul 2010	3.38	0.99	0.24
Woodland	7.302 W	40.238 N	31 Jul 2010	2.89	1.00	0.13
Grassland	0.870 W	34.014 N	31 Jul 2010	3.69	0.99	0.21
Cropland	4.576 W	37.446 N	31 Jul 2010	2.89	0.99	0.23
Unvegetated	7.490 E	32.600 N	31 Jul 2010	3.89	0.99	0.22

[a] SLP is the slope of LST versus local solar time.
[b] R^2 is the coefficient of determination.
[c] STD is the standard error of the estimate.

Table 2
Land cover classes before and after combination. The percent of each land cover class before combination over the study area is shown in parentheses.

IGBP class	Before combination	After combination
0	Water (48.27%)	–
1	Evergreen needleleaf forest (0.90%)	Forest
2	Evergreen broadleaf forest (0.04%)	
3	Deciduous needleleaf forest (0.01%)	
4	Deciduous broadleaf forest (0.42%)	
5	Mixed forest (4.60%)	
6	Closed shrublands (0.11%)	Shrubland
7	Open shrublands (7.22%)	
8	Woody savannas (3.63%)	Woodland
9	Savannas (0.69%)	
10	Grasslands (2.96%)	Grassland
11	Permanent wetlands (0.05%)	–
12	Croplands (12.55%)	Cropland
14	Cropland/natural vegetation mosaic (3.99%)	
15	Snow and ice (0.06%)	–
13	Urban and built-up (0.66%)	Unvegetated
16	Barren or sparsely vegetated (13.84%)	

open shrublands. Detailed information on the land cover types is shown in Table 2. The elevation of the study area ranges from − 103 to 4536 m.

2.2. DEM data

The global digital elevation model (DEM) data GTOPO30 were downloaded from the USGS website (http://eros.usgs.gov/). The GTOPO30 data cover the full extent of the longitudes from 180° W to 180° E and latitudes from 90° N to 90° S. The horizontal grid spacing is 30 arc-seconds (approximately 1 km). The horizontal coordinate system is decimal degrees of latitude, and the longitude is referenced to WGS84. The vertical units represent elevation in meters above mean sea level. In the DEM data, ocean areas are masked as "no data" and are assigned a value of − 9999. Four tiles (W020N90, E020N90, W020N40, and E020N40) covered the study area were used in this study. The GTOPO30 data were aggregated to the MSG-SEVIRI and MOD11A1 pixel scale in terms of longitude and latitude.

2.3. MODIS data

Three MODIS products were used in this study: (1) the MODIS/Terra Land Surface Temperature and Emissivity Daily L3 Global 1-km SIN Grid product (MOD11A1, Collection 5), (2) the MODIS/Terra Surface Reflectance Daily L2G Global 1-km and 500-m SIN Grid product (MOD09GA,

Collection 5), and (3) the MODIS Terra + Aqua Land Cover Type Yearly L3 Global 500-m SIN Grid product (MCD12Q1, Collection 5.1). These three MODIS products were downloaded from the Reverb website (http://reverb.echo.nasa.gov/).

The MOD11A1 product provides per-pixel LST and emissivity values at 1-km resolution using the generalized split-window algorithm (Wan & Dozier, 1996). LST, observation time (local solar time), and quality control during daytime were extracted from the MOD11A1 product. Only the pixels identified as clear sky over land were used in this study.

The MOD09GA product provides MODIS bands 1–7 of daily surface reflectance at 500-m resolution and observation and geolocation statistics at 1-km resolution (Vermote et al., 1997). The daily surface reflectance of bands 1 and 2 was extracted to calculate the daily NDVI. The solar zenith angle (SZA) at 1-km resolution was also extracted from the MOD09GA product. The NDVI and SZA were aggregated to the MSG-SEVIRI and MOD11A1 pixel scale in terms of longitude and latitude. Although the surface reflectance of the MSG-SEVIRI red and near infrared (NIR) channels can be used to calculate NDVI, it is difficult to obtain corresponding atmospheric parameters to derive surface reflectance from the MSG-SEVIRI data. Therefore, the surface reflectance of the MODIS red and NIR channels was used to calculate NDVI in this study.

The MCD12Q1 product contains five different land cover classification schemes (Friedl et al., 2010). The primary land cover scheme,
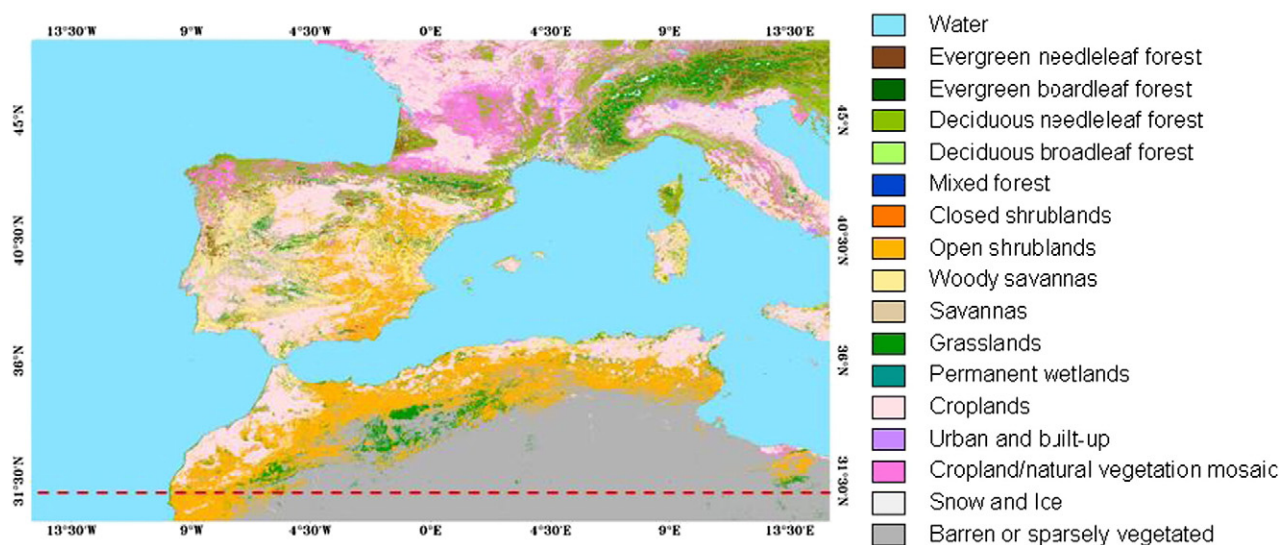

Fig. 3. Land cover types of the study area generated from the Collection 5.1 MODIS land cover type product MCD12Q1. All pixels in the dashed line were used to evaluate the differences between the LST before and after temporal normalization, as described in Section 4.5.

defined by the International Geosphere–Biosphere Programme (IGBP), was used in this study. To match the MSG-SEVIRI pixels, the MCD12Q1 pixels were aggregated to the MSG-SEVIRI pixel scale in terms of longitude and latitude. Each MSG-SEVIRI pixel was assigned to the dominant land cover class within this pixel according to the MCD12Q1 land cover class. The aggregated land cover classes were combined into six general land cover classes: forest, shrubland, woodland, grassland, cropland, and unvegetated land (see Table 2). The permanent wetland class and the snow and ice class were discarded because of their extremely small sample size over the study area. In addition, all ocean pixels defined by the land/water mask were excluded. The same procedures were also performed to aggregate the MCD12Q1 pixels at 500-m resolution to the MOD11A1 pixels at 1-km resolution.

2.4. MSG-SEVIRI data

Two MSG-SEVIRI products were used in this study: (1) the level-1.5 image data and (2) the cloud mask. These two MSG-SEVIRI products were downloaded from the European Organization for the Exploitation of Meteorological Satellites (EUMETSAT) Earth Observation Portal (EOP) website (https://eoportal.eumetsat.int/).

The level-1.5 image data are the geolocated and radiometrically pre-processed image data, which are stored as digital counts in binary files. The image data were converted into the top-of-the-atmosphere (TOA) brightness temperature in the MSG-SEVIRI channels 9 and 10 using the SEVIRI Pre-processing Toolbox (SPT) software. The MSG-SEVIRI LST was derived from the MSG-SEVIRI TOA brightness temperature in channels 9 and 10, using the algorithm proposed by Jiang, Li, and Nerry (2006) and Jiang and Li (2008).

The cloud mask product is an image-based product derived from the results of scene analysis. Each pixel is classified as one of the following four types: (1) cloudy, (2) clear sky over land, (3) clear sky over sea, and (4) not processed. Only the pixels identified as clear sky over land were used in this study.

3. Methodology

As shown in Fig. 2 and Table 1, there is a high correlation between LST and the local solar time during the period 10:00–12:00, with a coefficient of determination (R^2) greater than 0.94 for the in situ and MSG-SEVIRI-derived LST. Assuming that LST changes linearly with the local solar time during the period 10:00–12:00, the clear-sky Terra-MODIS LST during daytime can be normalized to a consistent local solar time (e.g., 11:00 local solar time) in terms of the slope of LST versus local solar time:

$$LST_{an} = (t_{an} - t_{bn})SLP + LST_{bn} \qquad (1)$$

where SLP is the slope of LST versus local solar time during the period 10:00–12:00, LST_{bn} is the LST before temporal normalization (i.e., the MODIS LST measurement), LST_{an} is the LST after temporal normalization, and t_{bn} and t_{an} are the local solar times corresponding to LST_{bn} and LST_{an}, respectively. In this study, the value of t_{an} was fixed at 11:00 local solar time.

To normalize the MODIS LST to a consistent local solar time using Eq. (1), one must first determine the SLP. Nevertheless, it is difficult to directly derive the SLP from the MODIS LST because only one MODIS measurement is available during the period 10:00–12:00 local solar time. Because the new generation of geostationary satellites, such as MSG-SEVIRI, can provide thermal infrared data every 15 min, MSG-SEVIRI-derived LST can be used to establish the relationship between the SLP and other parameters. In theory, a physical deterministic model that explains the spatial and temporal patterns of the SLP optimally involves many factors, such as incoming solar radiation, elevation, land cover, wind, and soil moisture (Hengl, Heuvelink, Perčec Tadić, & Pebesma, 2012). It is, however, difficult and impractical to collect data for so many parameters. Therefore, three available parameters, NDVI, SZA, and DEM, were taken into account in this study. NDVI, an index that has been found to be closely linked with land cover, vegetation density, and productivity, is included to account for the effect of different land cover types on the thermal processes of land surfaces. SZA reflects the difference in solar radiation in different zones. Elevation is recognized as an important factor in characterizing the variation in LST. A multiple linear regression model was developed to estimate the SLP from these three variables:

$$SLP = a_1 NDVI + a_2 \cos\theta_s + a_3 DEM + a_0 \qquad (2)$$

where a_0, a_1, a_2, and a_3 are the regression coefficients.

4. Results and discussion

4.1. Effect of different months on the SLP estimation

To examine the relationship between the SLP and the NDVI, SZA, and DEM, a random sample of 100 pixels was selected for each of the six general land cover classes for each day in January, April, July, and October 2010. A total of 18,600 or 18,000 pixels (i.e., 100 pixels × 6 classes × 31 or 30 days) for each month was used to analyze the effect of different months on the SLP estimation. Table 3 shows the regression equations and statistics of the SLP estimation for the different months. All of the regressions are statistically significant at the 99% confidence level. The adjusted coefficient of determination (R^2 adj) values range from 0.40 for January to 0.49 for April. The standard error of the estimate (STD) values range from 0.55 for July to 0.67 for January.

To evaluate the performance of these regression equations, a random sample of 150 pixels was selected from the remaining pixels (i.e., discarding the pixels used to establish the regression equations) for each class and each day in January, April, July, and October 2010. A total of 27,900 or 27,000 pixels (i.e., 150 pixels × 6 classes × 31 or 30 days) for each month was used to validate the ability of these regression equations to estimate the SLP. Fig. 4 shows the histograms of the differences between the actual SLP and the estimated SLP using the regression equations shown in Table 3 for January, April, July, and October. The root mean square error (RMSE) values of the SLP differences are 0.69, 0.61, 0.55, and 0.61 for January, April, July, and October, respectively. The best SLP estimation accuracy was obtained for July, whereas the worst accuracy was obtained for January. The range in the results is due to a large range in NDVI during the period of vegetation growth in July versus a small range in NDVI during the period of vegetation decay in January.

Table 3
Regression equations and statistics for SLP estimation for January, April, July, and October 2010.

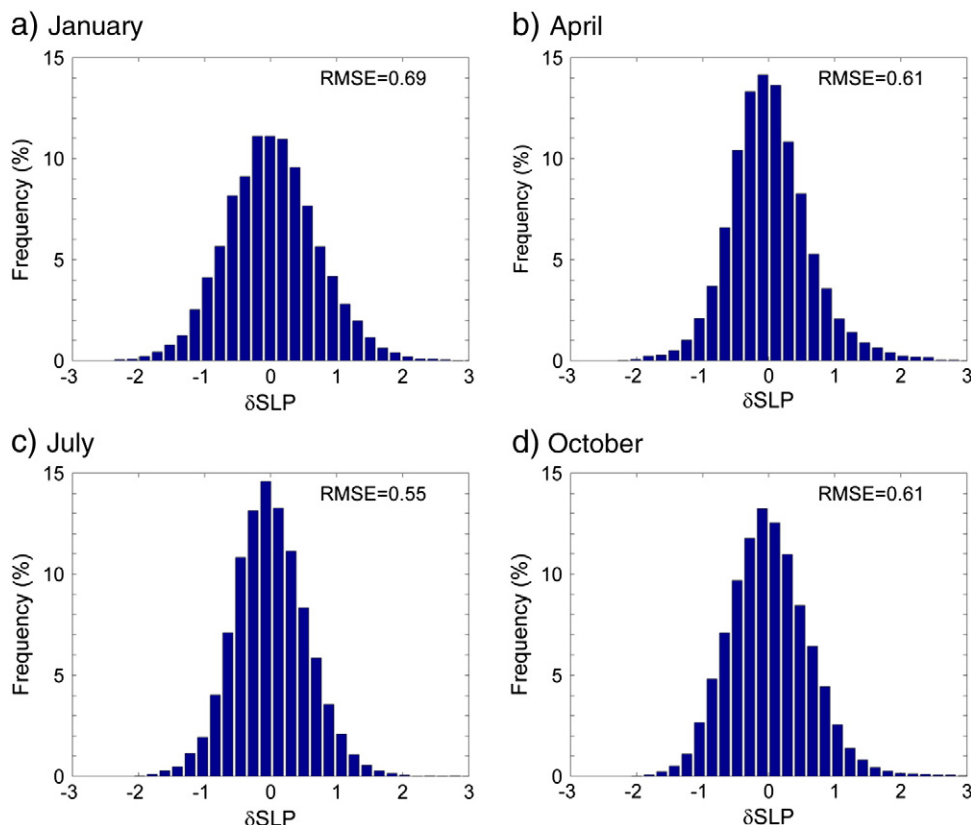| Month	Regression equation[a]	R^2 adj	STD	p-Value
January	$SLP = -1.605NDVI + 3.270\cos\theta_s + 0.187DEM + 1.801$	0.40	0.67	<0.001
April	$SLP = -2.559NDVI - 0.205\cos\theta_s + 0.148DEM + 3.935$	0.49	0.60	<0.001
July	$SLP = -2.191NDVI + 0.347\cos\theta_s + 0.037DEM + 3.096$	0.48	0.55	<0.001
October	$SLP = -1.014NDVI - 0.198\cos\theta_s + 0.204DEM + 3.110$	0.45	0.61	<0.001

[a] DEM in km

Fig. 4. Histograms of the differences between the actual *SLP* and the estimated *SLP* using the regression equations shown in Table 3 for (a) January, (b) April, (c) July, and (d) October 2010.

4.2. Effect of different land cover classes on the SLP estimation

To analyze the effect of different land cover classes on the *SLP* estimation, the selected 3100 pixels (i.e., 100 pixels × 31 days) for each class for July 2010 described in Section 4.1 were used to establish the regression equations for forest, shrubland, woodland, grassland, cropland, and unvegetated land. The regression equation established using the selected pixels of each class for July 2010 is referred to as a sub-class equation, whereas the equation established using the selected 18,600 pixels (i.e., 100 pixels × 6 classes × 31 days) of all classes for July 2010 (i.e., the third regression equation shown in Table 3) is referred to as the all-class equation.

The other selected 4650 pixels (i.e., 150 pixels × 31 days) of each class for July 2010 described in Section 4.1 were used to evaluate the performance of the all-class equation and the sub-class equation for each class. Fig. 5 displays the histograms of the differences between the actual *SLP* and the estimated *SLP* using the all-class equation and the sub-class equation for each class. Both histograms have similar distribution patterns for the *SLP* differences using the all-class equation and the sub-class equation for each class. The differences between the RMSE values of the *SLP* differences using the all-class equation and the sub-class equation for each class are almost negligible. These results indicate that it is not necessary to establish regression equations for the *SLP* for different land cover types. Nevertheless, as we can see from Fig. 2 and Table 1, the *SLP* is related to the land cover type. The value of the *SLP* increases from vegetation to bare soil. The insignificant differences in the *SLP* estimation using the all-class and sub-class equations may be due to the mixture of different land cover types in the MSG-SEVIRI pixels (3 km × 3 km at nadir).

4.3. Effect of different zones on the SLP estimation

To investigate the effect of different zones on the *SLP* estimation, the study area was divided into four zones (zone A: 15° W–0° E, 39°

N–48° N, zone B: 0° E–15° E, 39° N–48° N, zone C: 15° W–0° E, 30° N–39° N, and zone D: 0° E–15° E, 30° N–39° N). A random sample of 100 pixels was selected for each zone on each day in July 2010. The regression equation established using the selected 3100 pixels (i.e., 100 pixels × 31 days) of each zone is referred to as a sub-zone equation, whereas that established using the selected 18,600 pixels (i.e., 100 pixels × 6 classes × 31 days) of the whole study area (i.e., the third regression equation shown in Table 3) is referred to as the all-zone equation.

A random sample of 150 pixels was selected from the remaining pixels (i.e., discarding the pixels used to establish the sub-zone equations) for each zone on each day in July 2010. A total of 4650 pixels (i.e., 150 pixels × 31 days) for each zone was used to assess the performance of the all-zone equation and the sub-zone equation for each zone. Fig. 6 displays the histograms of the differences between the actual *SLP* and the estimated *SLP* using the all-zone equation and the sub-zone equation for each zone. The histograms have similar distribution patterns in the *SLP* differences using the all-zone equation and the sub-zone equation for each zone. There are no significant differences between the RMSE values of the *SLP* differences using the all-zone equation and the sub-zone equation for each zone. These results indicate that it is not necessary to establish regression equations for the *SLP* for different zones. In theory, the *SLP* is related to latitude, which reflects the variations of solar insolation in different zones. The insignificant differences in the *SLP* estimation using the all-zone and sub-zone equations may be due to the relatively small range of latitude of the study area.

4.4. Sensitivity analysis

The uncertainty of the proposed algorithm was evaluated with a sensitivity analysis. The uncertainty of the LST after temporal normalization (ΔLST_{an}) was estimated as the combination of the algorithm error (ΔLST_A), the uncertainty associated with the uncertainties of the
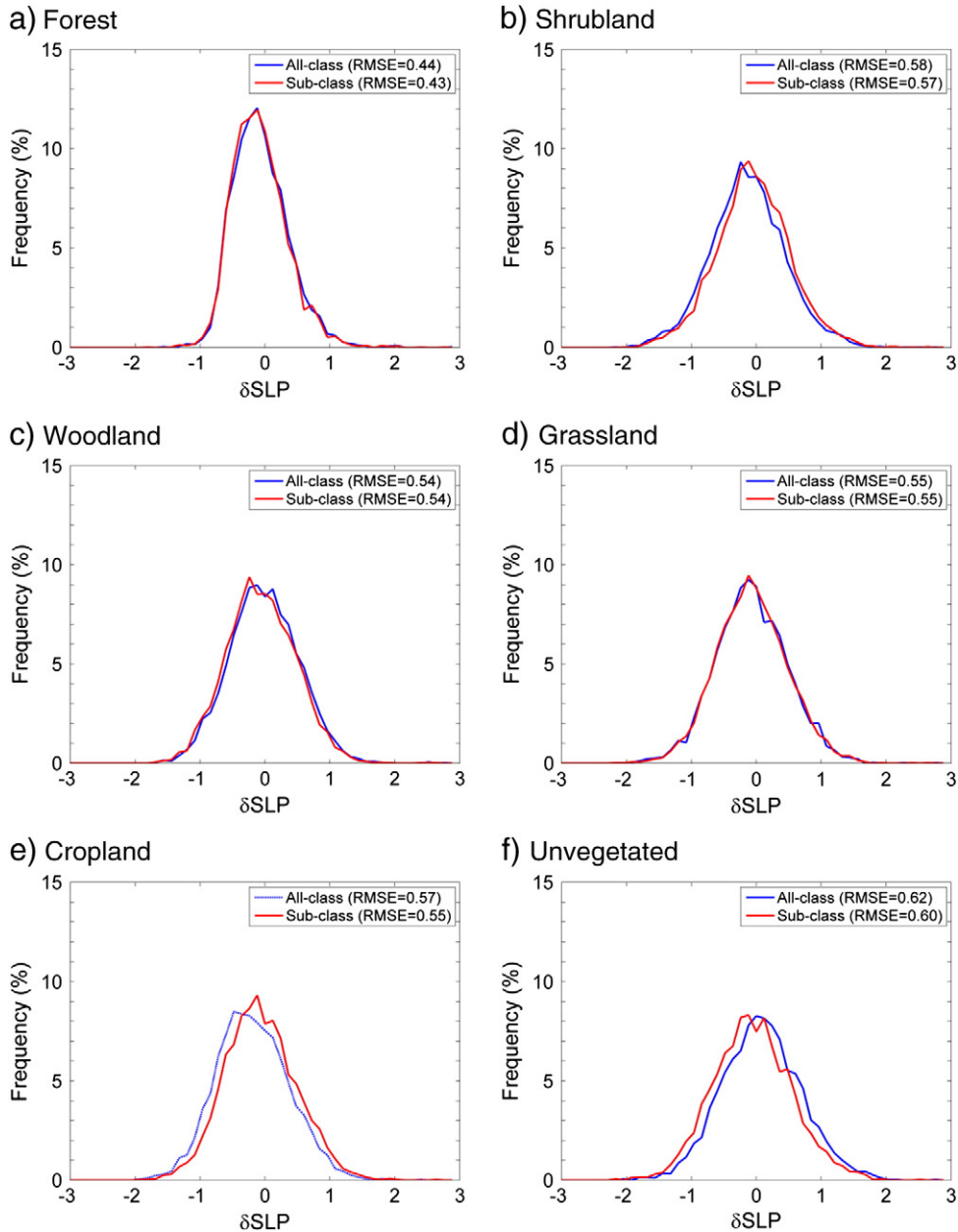
Fig. 5. Histograms of the differences between the actual *SLP* and the estimated *SLP* using the all-class equation and the sub-class equation for (a) forest, (b) shrubland, (c) woodland, (d) grassland, (e) cropland, and (f) unvegetated land. Sub-class represents the regression equation established using the selected pixels for each class for July 2010. All-class indicates the regression equation established using the selected pixels for all classes for July 2010.

input parameters (ΔLST_P), and the uncertainty of the LST before temporal normalization (ΔLST_{bn}):

$$\Delta LST_{an} = \left[\Delta LST_A^2 + \Delta LST_P^2 + \Delta LST_{bn}^2 \right]^{1/2} \quad (3)$$

with

$$\Delta LST_A = (11 - t_{bn})\Delta SLP \quad (4)$$

$$\Delta LST_P = (11 - t_{bn})\left[(a_1 \Delta NDVI)^2 + (a_2 \Delta SZA)^2 + (a_3 \Delta DEM)^2 \right]^{1/2} \quad (5)$$

where ΔSLP is the fitting error of the *SLP*; $\Delta NDVI$, ΔSZA, and ΔDEM are the uncertainties of NDVI, SZA, and DEM, respectively; and a_1, a_2, and a_3 are the regression coefficients.

According to Wan et al. (2002, 2004), the accuracy of the MODIS LST is approximately 1 K. As shown in Fig. 4 and Table 3, the fitting error of

the *SLP* is approximately 0.7. The uncertainty of DEM is approximately 0.03 km, and the uncertainty of SZA is assumed to be negligible. The uncertainty of NDVI is a function of both the red and NIR reflectance and can be expressed as follows:

$$\Delta NDVI = \left[\left(\frac{2\rho_{NIR}}{(\rho_{red} + \rho_{NIR})^2} \Delta\rho_{red} \right)^2 + \left(\frac{2\rho_{red}}{(\rho_{red} + \rho_{NIR})^2} \Delta\rho_{NIR} \right)^2 \right]^{1/2} \quad (6)$$

where ρ_{red} and ρ_{NIR} are the red and NIR reflectance, respectively, and $\Delta\rho_{red}$ and $\Delta\rho_{NIR}$ are the uncertainties of the red and NIR reflectance, respectively.

According to Vermote, Kotchenova, and Ray (2011), the accuracy of the MODIS reflectance is approximately $0.005 + 0.05 \times$ reflectance. Assuming that the values of the red and NIR reflectance are approximately 0.1 and 0.4, respectively, and the uncertainties of the red and NIR reflectance are 0.01 and 0.025, respectively. The values of ΔLST_{an} can be calculated using Eqs. (3)–(6). Fig. 7 displays the values of
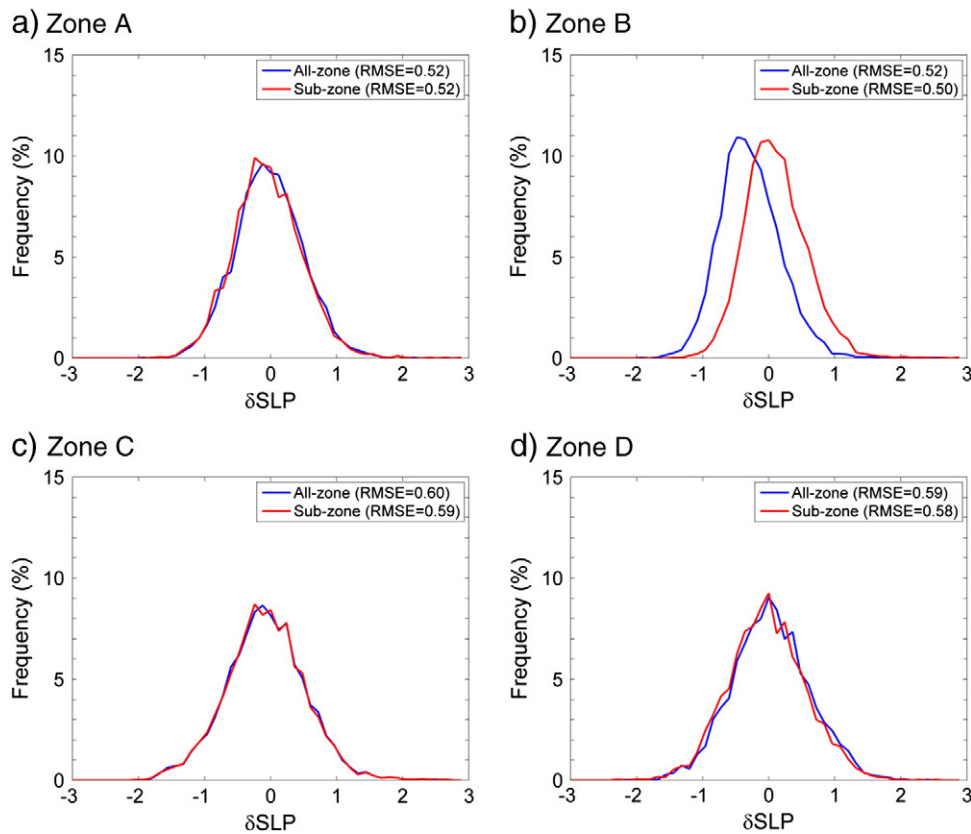
Fig. 6. Histograms of the differences between the actual *SLP* and the estimated *SLP* using the all-zone equation and the sub-zone equation for (a) zone A, (b) zone B, (c) zone C, and (d) zone D. Sub-zone represents the regression equation established using the selected pixels for each zone for July 2010. All-zone indicates the regression equation established using the selected pixels for the whole study area for July 2010.

ΔLST_{an} versus local solar time for July. There are no significant differences among the values of ΔLST_{an} for different months. The values of ΔLST_{an} are better than 1.3 K during the period 10:00–12:00 local solar time. It should be kept in mind that the values of ΔLST_{an} depend on the accuracy of the LST before temporal normalization. In this study, the accuracy of the LST before temporal normalization is assumed to be 1 K, which accounts for approximately 80% of the total error. Therefore, the uncertainty of the LST after temporal normalization is mainly due to the uncertainty of the LST before temporal normalization, whereas that caused by the algorithm error and the uncertainties of the input parameters is very small.
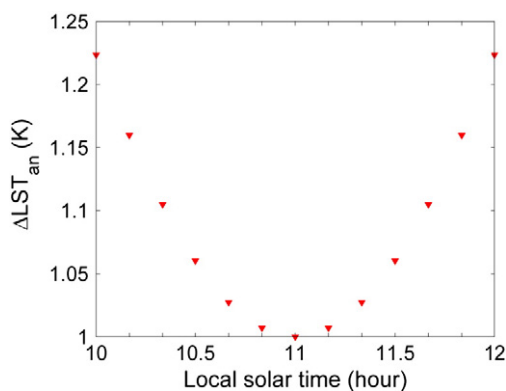

Fig. 7. Uncertainty of the LST after temporal normalization (ΔLST_{an}) versus local solar time during the period 10:00–12:00.

4.5. Accuracy assessment of algorithm

Because the MSG-SEVIRI can provide the diurnal cycle of LST, the MSG-SEVIRI-derived LST for four clear-sky days – 2 January, 10 April, 31 July, and 1 October 2010 – was used to evaluate the accuracy of the proposed algorithm. Taking into account the crossing time of the Terra-MODIS over the study area, the MSG-SEVIRI-derived LST at 11:00 UTC was represented by the LST before temporal normalization (LST_{bn}). The local solar time (local solar time = UTC + longitude / 15) of each pixel over the study area is thus between 10:00 and 12:00. The MSG-SEVIRI-derived LST at 11:00 UTC was normalized to 11:00 local solar time using Eq. (1). The values of the *SLP* for each pixel were estimated using the regression equations shown in Table 3. The normalized LST at 11:00 local solar time was denoted by LST_{an}. To derive the actual LST at 11:00 local solar time for each pixel, the diurnal cycle of the MSG-SEVIRI-derived LST was fitted using the DTC model, improved by Duan et al. (2013). The LST modeled by the DTC model at 11:00 local solar time was prescribed as the actual LST (LST_{act}). All cloud-free pixels over the study area were divided into 12 groups in 10-minute increments during the period 10:00–12:00 local solar time. A random sample of 100 pixels was selected from each of the 12 groups. The selected pixels from all groups were then used to calculate δLST_{bn} ($\delta LST_{bn} = LST_{bn} - LST_{act}$) and δLST_{an} ($\delta LST_{an} = LST_{an} - LST_{act}$). Fig. 8 shows the histograms of δLST_{bn} and δLST_{an} on 2 January, 10 April, 31 July, and 1 October 2010. The RMSE values of δLST_{bn} and δLST_{an} are 1.57 (0.52), 1.29 (0.47), 1.50 (0.47), and 1.51 (0.57) K on 2 January, 10 April, 31 July, and 1 October 2010, respectively.

To analyze whether the regression equations of the *SLP* established using the data for 2010 can be used to normalize the LST in other years, the MSG-SEVIRI-derived LST of four clear-sky days – 20 January, 26 April, 3 July, and 26 October 2008 – was selected. Fig. 9 shows the
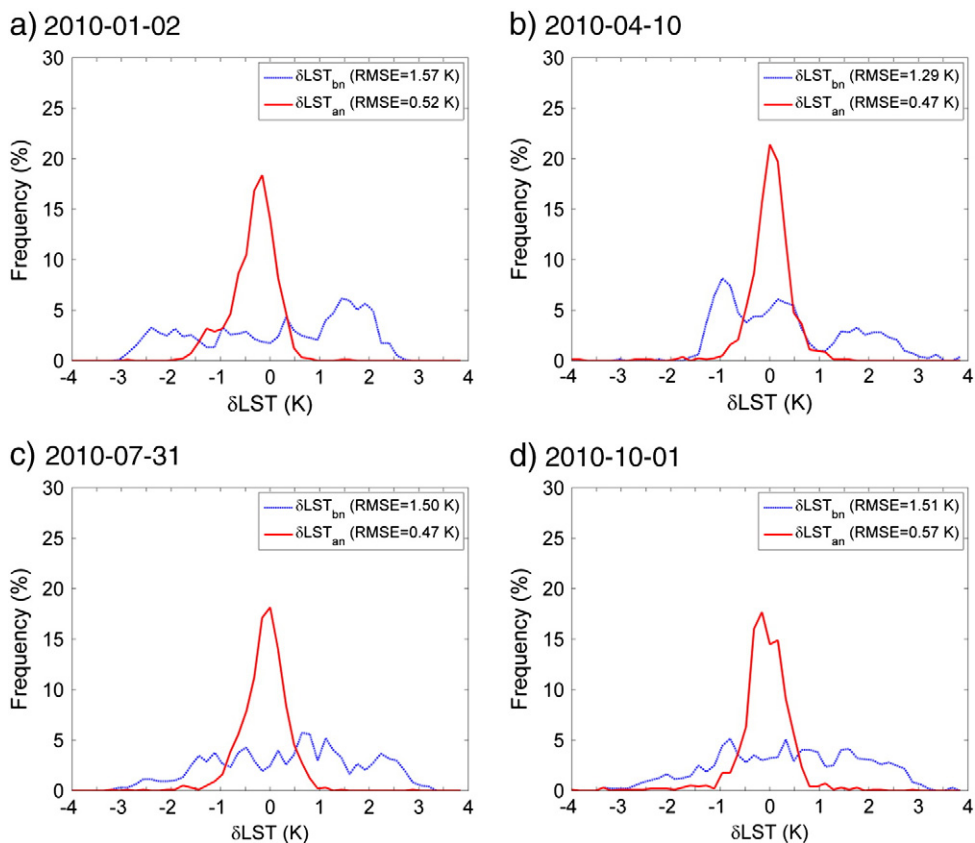
Fig. 8. Histograms of the differences between the actual LST (LST_{act}) and the LST before temporal normalization (LST_{bn}), as well as the LST after temporal normalization (LST_{an}), on (a) 2 January, (b) 10 April, (c) 31 July, and (d) 1 October 2010. $\delta LST_{bn} = LST_{bn} - LST_{act}$, and $\delta LST_{an} = LST_{an} - LST_{act}$.
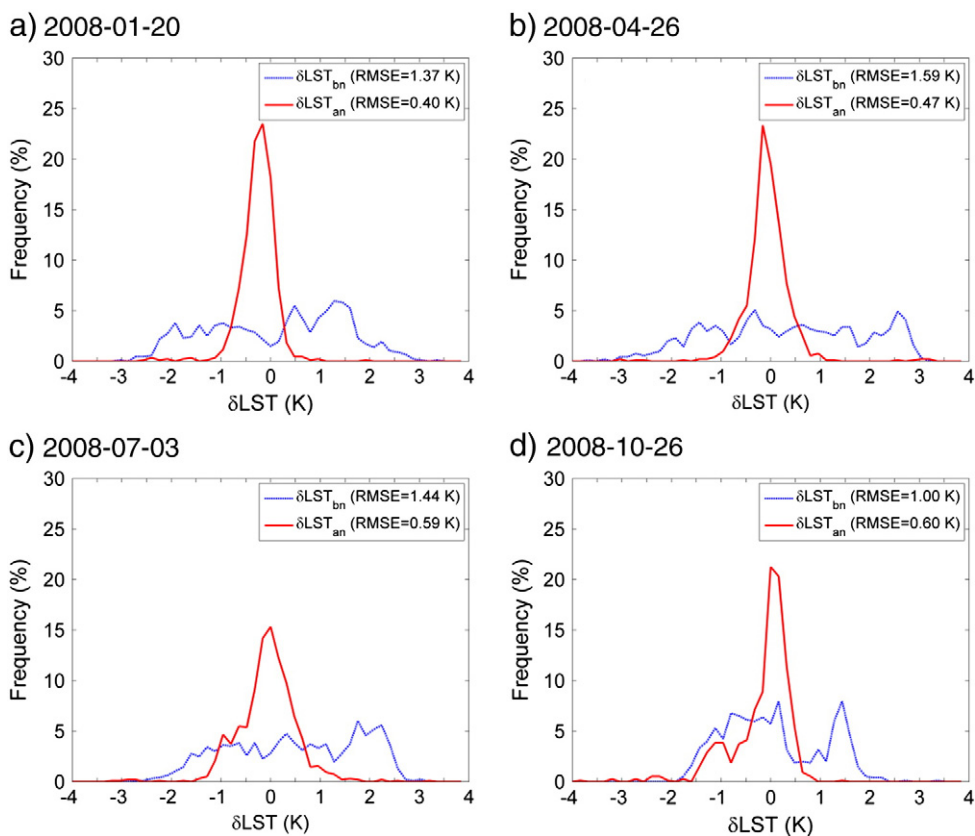

Fig. 9. Histograms of the differences between the actual LST (LST_{act}) and the LST before temporal normalization (LST_{bn}), as well as the LST after temporal normalization (LST_{an}), on (a) 20 January, (b) 26 April, (c) 3 July, and (d) 26 October 2008. $\delta LST_{bn} = LST_{bn} - LST_{act}$, and $\delta LST_{an} = LST_{an} - LST_{act}$.

histograms of δLST_{bn} and δLST_{an} for 20 January, 26 April, 3 July, and 26 October 2008. The RMSE values of δLST_{bn} and δLST_{an} are 1.37 (0.40), 1.59 (0.47), 1.44 (0.59), and 1.00 (0.60) K for 20 January, 26 April, 3 July, and 26 October 2008, respectively. Comparing Fig. 9 with Fig. 8, the accuracies of the LST before and after normalization for 2008 are similar to those for 2010. These results demonstrate that the regression equations with the *SLP* established using the data in 2010 can be used to normalize the LST in other years.

All cloud-free pixels in the horizontal profile shown in Fig. 3 were selected as examples to compare δLST_{bn} and δLST_{an}. Fig. 10 displays δLST_{bn} and δLST_{an} versus local solar time during the period 10:00–12:00 on 31 July 2010. The values of δLST_{bn} range from approximately −2.5 to 3 K, whereas those of δLST_{an} range from approximately −1 to 1 K.

To further investigate the discrepancies between the LST before and after temporal normalization, the RMSE values of δLST_{bn} and δLST_{an} versus local solar time during the period 10:00–12:00 were calculated. All cloud-free pixels over the study area were divided into 12 groups in 10-minute increments during the period 10:00–12:00 local solar time. A random sample of 100 pixels was selected from each of the 12 groups. The selected pixels of all groups were then used to calculate the RMSE values of δLST_{bn} and δLST_{an}. Fig. 11 shows the RMSE values of δLST_{bn} and δLST_{an} versus local solar time during the period 10:00–12:00 on 31 July 2010. The RMSE values of δLST_{bn} range from approximately 0.5 to 2.5 K, whereas those of δLST_{an} range from approximately 0.5 to 1 K.

4.6. Application to MODIS data

Assuming that the MODIS LST exhibits similar variation pattern to the MSG-SEVIRI-derived LST during the period 10:00–12:00 local solar time, the proposed method was used to normalize the Terra-MODIS LST during daytime to a consistent local solar time (i.e., 11:00 local solar time). As mentioned previously, the uncertainty of the LST after temporal normalization caused by the algorithm error and the uncertainties of the input parameters is very small. Therefore, the *SLP* determined by the MSG-SEVIRI data can be applied to the temporal normalization of the MODIS LST. As an example, the Terra-MODIS LST on 31 July 2010 was used to perform the temporal normalization of LST. Fig. 12a and b displays the Terra-MODIS LST before and after temporal normalization. A comparison of Fig. 12b with Fig. 12a shows that the spatial variations in the LST after temporal normalization appear to be more uniform than those in the LST before temporal normalization. Fig. 12c presents the differences between the LST before and after temporal normalization. The LST differences range from −2 to 4 K. Fig. 12d shows the observation time of the Terra-MODIS LST before temporal normalization. A comparison of Fig. 12c with Fig. 12d shows that the LST differences are significantly related to the observation time.
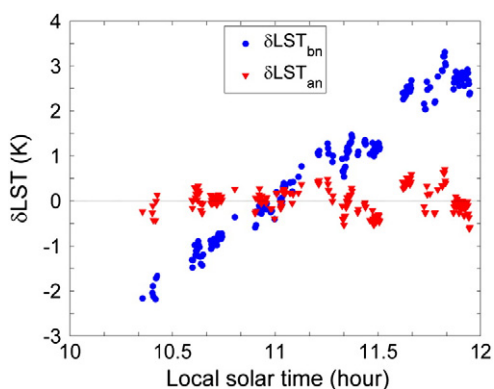
Fig. 10. Differences between the actual LST (LST_{act}) and the LST before temporal normalization (LST_{bn}), as well as the LST after temporal normalization (LST_{an}) versus the local solar time during the period 10:00–12:00 on 31 July 2010. $\delta LST_{bn} = LST_{bn} - LST_{act}$, and $\delta LST_{an} = LST_{an} - LST_{act}$.
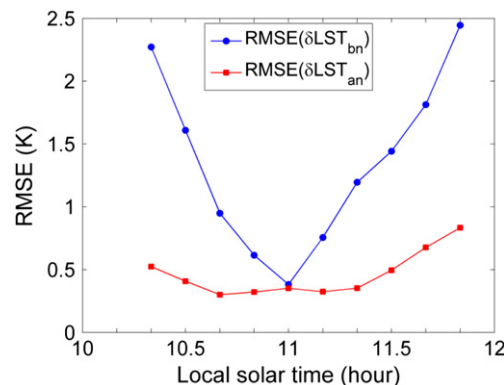
Fig. 11. RMSE values of the differences between the actual LST (LST_{act}) and the LST before temporal normalization (LST_{bn}), as well as the LST after temporal normalization (LST_{an}) versus local solar time during the period 10:00–12:00 on 31 July 2010. $\delta LST_{bn} = LST_{bn} - LST_{act}$, and $\delta LST_{an} = LST_{an} - LST_{act}$.

The Terra-MODIS LST of six pixels for forest, shrubland, woodland, grassland, cropland, and unvegetated land in July 2010 was selected as examples to illustrate the differences between the LST before and after temporal normalization versus local solar time. These results are shown in Fig. 13. The LST differences change nearly linearly with local solar time. The LST differences range from approximately −1 to 2 K for the forest, woodland, and cropland pixels, whereas those range from approximately −2 to 3 K for the shrubland, grassland, and unvegetated land pixels. These results indicate that the *SLP* values of the shrubland, grassland, and unvegetated land pixels are greater than those of the forest, woodland, and cropland pixels, as illustrated in Fig. 2 and Table 1.

The normalized LST is not validated because of the lack of in situ data or remotely sensed data from another source. Validation of LST at the satellite pixel scale is challenging because LST can vary significantly within a pixel and change within relatively short time periods. In addition, the number of in situ measurements that match satellite observations in both time and space is limited. It should be kept in mind that the normalized LST is only time-consistent, not angle-consistent. The view angle of the LST after temporal normalization is the same as that of the LST before temporal normalization. In theory, the Terra-MODIS LST should be normalized to the same view angle (e.g., at nadir) before the temporal normalization of LST. Although the literature reports that directional effects (angular anisotropy) in the LST have been demonstrated or simulated at the satellite pixel scale (Otterman et al., 1997; Pinheiro, Privette, & Guillevic, 2006; Pinheiro, Privette, Mahoney, & Tucker, 2004; Rasmussen, Göttsche, Olesen, & Sandholt, 2011; Rasmussen, Pinheiro, Proud, & Sandholt, 2010; Ren, Yan, Chen, & Li, 2011; Vinnikov et al., 2012), there is not any practical way to perform angular normalization of satellite-derived LST, because of the complexity of this normalization.

5. Conclusions

A method for the temporal normalization of the Terra-MODIS LST during the day was developed to generate a time-consistent LST product. This method uses the slope of LST versus the local solar time during the period 10:00–12:00 to normalize the Terra-MODIS LST to a consistent local solar time (e.g., 11:00 local solar time). A multiple linear regression model for *SLP* as a function of three variables (NDVI, SZA, and DEM) was established using the MSG-SEVIRI data. The influences of different months, land cover types, and zones on the *SLP* estimation were investigated. The results indicate that it is not necessary to establish the regression equations for *SLP* for different land cover types and zones. The soil moisture and diurnal temperature range may be used to further improve the accuracy of the *SLP* estimation. Nevertheless, soil moisture and
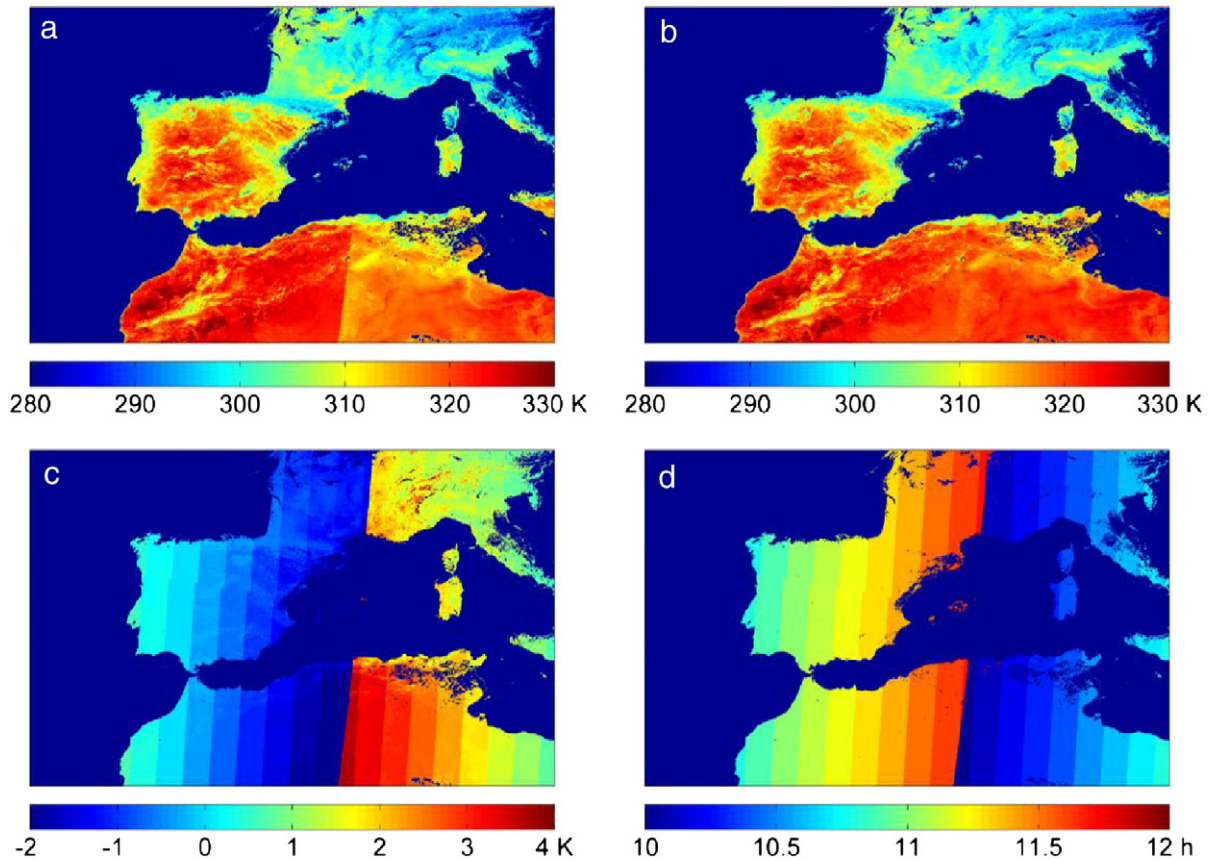
Fig. 12. Terra-MODIS LST (a) before and (b) after temporal normalization, (c) their differences, and (d) observation time on 31 July 2010.

diurnal temperature range products at the MODIS pixel scale are not available at this stage.

A sensitivity analysis of the algorithm was performed to assess the algorithm error, the uncertainties of the input parameters, and the uncertainty of the LST before temporal normalization. The uncertainty of the LST after temporal normalization is better than 1.3 K when the accuracy of the LST before temporal normalization is assumed to be 1 K. The uncertainty of the LST after temporal normalization is mainly caused by the uncertainty of the LST before temporal normalization. The contributions of the algorithm error and the uncertainties of the input parameters to the total errors are less than 20%.

The accuracy of the algorithm was evaluated using the MSG-SEVIRI-derived LST. The RMSE values of the differences between the actual LST and the LST before temporal normalization are approximately 1.5 K,

whereas those between the actual LST and the LST after temporal normalization are approximately 0.5 K. The regression equation established using the data for 2010 was applied to normalize the LST in 2008. The results indicate that similar accuracies for the LST after temporal normalization are achieved for the LST in 2008.

The method was used to normalize the Terra-MODIS LST during daytime to a consistent local solar time (i.e., 11:00 local solar time). A comparison of the LST before and after temporal normalization indicates that the spatial variations in the LST after temporal normalization appear more uniform than those in the LST before temporal normalization. The differences between the Terra-MODIS LST before and after temporal normalization range from −2 to 4 K and are significantly related to the LST observation time. The differences in the shrubland, grassland, and unvegetated classes are greater than those in the forest, woodland, and cropland classes due to the larger values of the *SLP* in the shrubland, grassland, and unvegetated classes.

Although this method was developed for the Terra-MODIS sensor, it can be extended to the temporal normalization of the LST of the other similar sensors onboard the polar-orbiting satellites, such as the NOAA-AVHRR and National Polar Orbiting Environmental Sensor Suite (NPOESS) Preparatory Project (NPP)-Visible Infrared Imager Radiometer Sensor (VIIRS). A long-term and time-consistent climate data record (CDR) and Earth system data record (ESDR) can thus be generated from the measurements of the AVHRR, MODIS, and VIIRS. Nevertheless, prior to the generation of the CDR and ESDR, co-calibration of the AVHRR, MODIS, and VIIRS is necessary.
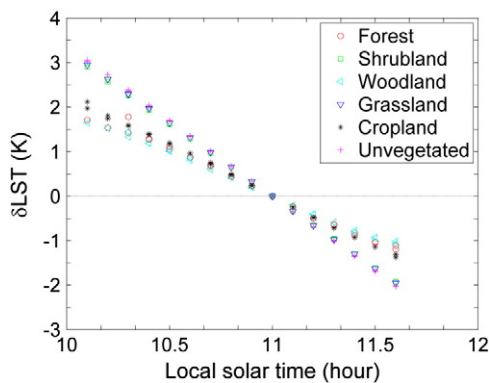
Acknowledgments

Fig. 13. Differences between the Terra-MODIS LST before and after temporal normalization versus local solar time for forest, shrubland, woodland, grassland, cropland, and unvegetated pixels for July 2010. $\delta LST = LST_{an} - LST_{bn}$.

References

Aires, F., Prigent, C., & Rossow, W. (2004). Temporal interpolation of global surface skin temperature diurnal cycle over land under clear and cloudy conditions. *Journal of Geophysical Research*, *109*, 1–18.

Anderson, M. C., Norman, J. M., Kustas, W. P., Houborg, R., Starks, P. J., & Agam, N. (2008). A thermal-based remote sensing technique for routine mapping of land-surface carbon, water and energy fluxes from field to regional scales. *Remote Sensing of Environment*, *112*, 4227–4241.

Becker, F., & Li, Z. -L. (1990). Towards a local split window method over land surfaces. *International Journal of Remote Sensing*, *11*, 369–393.

Coll, C., Wan, Z., & Galve, J. M. (2009). Temperature-based and radiance-based validations of the V5 MODIS land surface temperature product. *Journal of Geophysical Research*, *114*, D20102. http://dx.doi.org/10.1029/2009JD012038.

Duan, S. -B., Li, Z. -L., Wang, N., Wu, H., & Tang, B. -H. (2012). Evaluation of six land-surface diurnal temperature cycle models using clear-sky *in situ* and satellite data. *Remote Sensing of Environment*, *124*, 15–25.

Duan, S. -B., Li, Z. -L., Wu, H., Tang, B. -H., Jiang, X., & Zhou, G. (2013). Modeling of day-to-day temporal progression of clear-sky land surface temperature. *IEEE Geoscience and Remote Sensing Letters*, *10*, 1050–1054.

Friedl, M.A., Sulla-Menashe, D., Tan, B., Schneider, A., Ramankutty, N., Sibley, A., et al. (2010). MODIS Collection 5 global land cover: Algorithm refinements and characterization of new datasets. *Remote Sensing of Environment*, *114*, 168–182.

Göttsche, F. -M., & Olesen, F. -S. (2001). Modelling of diurnal cycles of brightness temperature extracted from METEOSAT data. *Remote Sensing of Environment*, *76*, 337–348.

Göttsche, F. -M., & Olesen, F. -S. (2009). Modelling the effect of optical thickness on diurnal cycles of land surface temperature. *Remote Sensing of Environment*, *113*, 2306–2316.

Hengl, T., Heuvelink, G. B.M., Perčec Tadić, M., & Pebesma, E. J. (2012). Spatio-temporal prediction of daily temperatures using time-series of MODIS LST images. *Theoretical and Applied Climatology*, *107*, 265–277.

Inamdar, A. K., & French, A. (2009). Disaggregation of GOES land surface temperatures using surface emissivity. *Geophysical Research Letters*, *36*, L02408. http://dx.doi.org/10.1029/2008GL036544.

Inamdar, A. K., French, A., Hook, S., Vaughan, G., & Luckett, W. (2008). Land surface temperature retrieval at high spatial and temporal resolutions over the southwestern United States. *Journal of Geophysical Research*, *113*, D07107. http://dx.doi.org/10.1029/2007JD009048.

Jiang, G., & Li, Z. -L. (2008). Split-window algorithm for land surface temperature estimation from MSG1-SEVIRI data. *International Journal of Remote Sensing*, *29*, 6067–6074.

Jiang, G., Li, Z. -L., & Nerry, F. (2006). Land surface emissivity retrieval from combined mid-infrared and thermal infrared data of MSG-SEVIRI. *Remote Sensing of Environment*, *105*, 326–340.

Jin, M., & Dickinson, R. E. (1999). Interpolation of surface radiative temperature measured from polar orbiting satellites to a diurnal cycle 1. Without clouds. *Journal of Geophysical Research*, *104*, 2105–2116.

Jin, M., & Dickinson, R. E. (2002). New observational evidence for global warming from satellite. *Geophysical Research Letters*, *29*. http://dx.doi.org/10.1029/2001GL013833.

Jin, M., & Treadon, R. E. (2003). Correcting the orbit drift effect on AVHRR land surface skin temperature measurements. *International Journal of Remote Sensing*, *24*, 4543–4558.

Karnieli, A., Agam, N., Pinker, R. T., Anderson, M., Imhoff, M. L., & Gutman, G. G. (2010). Use of NDVI and land surface temperature for drought assessment: Merits and limitations. *Journal of Climate*, *23*, 618–633.

Li, Z. -L., & Becker, F. (1993). Feasibility of land surface temperature and emissivity determination from AVHRR data. *Remote Sensing of Environment*, *43*, 67–85.

Li, Z. -L., Tang, R., Wan, Z., Bi, Y., Zhou, C., Tang, B., et al. (2009). A review of current methodologies for regional evapotranspiration estimation from remotely sensed data. *Sensors*, *9*, 3801–3853.

Li, Z. -L., Tang, B. -H., Wu, H., Ren, H., Yan, G., Wan, Z., et al. (2013a). Satellite-derived land surface temperature: Current status and perspectives. *Remote Sensing of Environment*, *131*, 14–37.

Li, Z. -L., Wu, H., Wang, N., Qiu, S., Sobrino, J. A., Wan, Z., et al. (2013b). Land surface emissivity retrieval from satellite data. *International Journal of Remote Sensing*, *34*, 3084–3127.

Mialon, A., Royer, A., Fily, M., & Picard, G. (2007). Daily microwave-derived surface temperature over Canada/Alaska. *American Meteorological Society*, *46*, 591–604.

Otterman, J., Starr, D., Brakke, T., Davies, R., Jacobowitz, H., Mehta, A., et al. (1997). Modeling zenith-angle dependence of outgoing longwave radiation: Implication for flux measurements. *Remote Sensing of Environment*, *62*, 90–100.

Pinheiro, A.C. T., Privette, J. L., & Guillevic, P. (2006). Modeling the observed angular anisotropy of land surface temperature in a Savanna. *IEEE Transactions on Geoscience and Remote Sensing*, *44*, 1036–1047.

Pinheiro, A.C. T., Privette, J. L., Mahoney, R., & Tucker, C. J. (2004). Directional effects in a daily AVHRR land surface temperature dataset over Africa. *IEEE Transactions on Geoscience and Remote Sensing*, *42*, 1941–1954.

Rasmussen, M.O., Göttsche, F. -M., Olesen, F. -S., & Sandholt, I. (2011). Directional effects on land surface temperature estimation from Meteosat Second Generation for Savanna landscapes. *IEEE Transactions on Geoscience and Remote Sensing*, *49*, 4458–4468.

Rasmussen, M.O., Pinheiro, A.C. T., Proud, S. R., & Sandholt, I. (2010). Modeling angular dependences in land surface temperature from the SEVIRI instrument onboard the Geostationary Meteosat Second Generation satellites. *IEEE Transactions on Geoscience and Remote Sensing*, *48*, 3123–3133.

Ren, H., Yan, G., Chen, L., & Li, Z. -L. (2011). Angular effect of MODIS emissivity products and its application to the split-window algorithm. *ISPRS Journal of Photogrammetry and Remote Sensing*, *66*, 498–507.

Schädlich, S., Göttsche, F. -M., & Olesen, F. -S. (2001). Influence of land surface parameters and atmosphere on METEOSAT brightness temperatures and generation of land surface temperature maps by temporally and spatially interpolating atmospheric correction. *Remote Sensing of Environment*, *75*, 39–46.

Sun, D., & Pinker, R. (2005). Implementation of GOES-based land surface temperature diurnal cycle to AVHRR. *International Journal of Remote Sensing*, *26*, 3975–3984.

Tang, B., & Li, Z. -L. (2008). Estimation of instantaneous net surface longwave radiation from MODIS cloud-free data. *Remote Sensing of Environment*, *112*, 3482–3492.

Tang, R., Li, Z. -L., & Tang, B. (2010). An application of the Ta-VI triangle method with enhanced edges determination for evapotranspiration estimation from MODIS data in arid and semi-arid regions: Implementation and validation. *Remote Sensing of Environment*, *112*, 540–551.

Vermote, E. F., El Saleous, N. Z., Justice, C. O., Kaufman, Y. J., Privette, J., Remer, L., et al. (1997). Atmospheric correction of visible to middle infrared EOS-MODIS data over land surface, background, operational algorithm and validation. *Journal of Geophysical Research*, *102*, 17131–17141.

Vermote, E. F., Kotchenova, S. Y., & Ray, J. P. (2011). *MODIS surface reflectance user's guide (version 1.3)*. MODIS Land Surface Reflectance Science Computing Facility (http://modis-sr.ltdri.org)

Vinnikov, K. Y., Yu, Y., Goldberg, M.D., Tarpley, D., Romanov, P., Laszlo, I., et al. (2012). Angular anisotropy of satellite observations of land surface temperature. *Geophysical Research Letters*, *39*, L23802. http://dx.doi.org/10.1029/2012GL054059.

Wan, Z. (2008). New refinements and validation of the MODIS land-surface temperature/emissivity products. *Remote Sensing of Environment*, *112*, 59–74.

Wan, Z., & Dozier, J. (1996). A generalized split-window algorithm for retrieving land-surface temperature from space. *IEEE Transactions on Geoscience and Remote Sensing*, *34*, 892–905.

Wan, Z., & Li, Z. -L. (1997). A physics-based algorithm for retrieving land-surface emissivity and temperature from EOS/MODIS data. *IEEE Transactions on Geoscience and Remote Sensing*, *35*, 980–996.

Wan, Z., & Li, Z. -L. (2008). Radiance-based validation of the V5 MODIS land-surface temperature product. *International Journal of Remote Sensing*, *29*, 5373–5395.

Wan, Z., Zhang, Y., Zhang, Q., & Li, Z. -L. (2002). Validation of the land-surface temperature products retrieved from Terra Moderate Resolution Imaging Spectroradiometer data. *Remote Sensing of Environment*, *83*, 163–180.

Wan, Z., Zhang, Y., Zhang, Q., & Li, Z. -L. (2004). Quality assessment and validation of the MODIS global land surface temperature. *International Journal of Remote Sensing*, *25*, 261–274.

Wang, W., Liang, S., & Meyers, T. (2008). Validating MODIS land surface temperature products using long-term nighttime ground measurements. *Remote Sensing of Environment*, *112*, 623–635.

Wang, K., Wan, Z., Wang, P., Sparrow, M., Liu, J., Zhou, X., et al. (2005). Estimation of surface long wave radiation and broadband emissivity using Moderate Resolution Imaging Spectroradiometer (MODIS) land surface temperature/emissivity products. *Journal of Geophysical Research*, *110*, D11109. http://dx.doi.org/10.1029/2004JD005566.